

Attention-Guided Perturbation for Unsupervised Image Anomaly Detection

Tingfeng Huang*, Yuxuan Cheng*, Jingbo Xia, Rui Yu, Yuxuan Cai, Jinghai Xiang, Xinwei He†, Xiang Bai, *Senior Member, IEEE*

Abstract—Reconstruction-based methods have significantly advanced modern unsupervised anomaly detection. However, the strong capacity of neural networks often violates the underlying assumptions by reconstructing abnormal samples well. To alleviate this issue, we present a simple yet effective reconstruction framework named Attention-Guided Perturbation Network (AGP-Net), which learns to add perturbation noise with an attention mask, for accurate unsupervised anomaly detection. Specifically, it consists of two branches, *i.e.*, a plain reconstruction branch and an auxiliary attention-based perturbation branch. The reconstruction branch is simply a plain reconstruction network that learns to reconstruct normal samples, while the auxiliary branch aims to produce attention masks to guide the noise perturbation process for normal samples from easy to hard. By doing so, we are expecting to synthesize hard yet more informative anomalies for training, which enable the reconstruction branch to learn important inherent normal patterns both comprehensively and efficiently. Extensive experiments are conducted on three popular benchmarks covering MVTec-AD, VisA, and MVTec-3D, and show that our framework obtains leading anomaly detection performance under various setups including few-shot, one-class, and multi-class setups.

Index Terms—Image Anomaly Detection, Reconstruction, Noise

I. INTRODUCTION

Automatically detecting and localizing anomalies in images, *i.e.*, visual anomaly detection (VAD), has extensive applications in manufacturing [1], [2]. However, this task typically encounters the challenge of *cold-start* [3] where gathering normal samples is easy, whereas acquiring anomalous samples is costly or infeasible, which prohibits supervised learning. Therefore, significant effort has been devoted to developing unsupervised anomaly detection (UAD) algorithms [4]–[9] that learn to model normality distribution with *solely* normal images. Among existing UAD works, reconstruction-based methods [10], [11] hold great promise and have been extensively

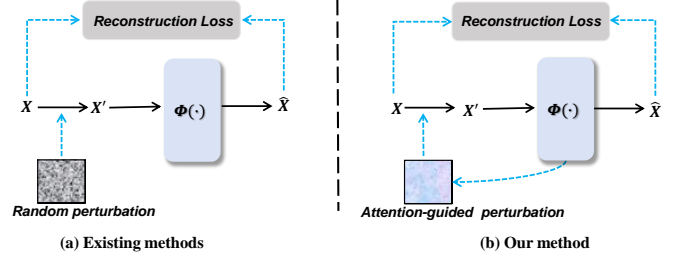


Fig. 1. Comparisons between our and existing perturbation strategies in reconstruction paradigm for anomaly detection. Compared with (a) existing networks adopting fixed or random perturbations, (b) we introduce to learn to guide the perturbation with sample-aware masks from the network and help to learn a better reconstruction model.

studied. Generally, they assume that reconstruction networks exposed to normal-only training images can reconstruct normal ones well, but find difficulty in reconstructing abnormal ones. Thus, an anomaly map can be computed by analyzing the reconstruction error between the input and its reconstructed counterpart. As per this assumption, some methods attempt to reconstruct input images with popular generative models, *e.g.*, AutoEncoder [4], [12], [13], GANs [14]–[16], or Diffusion-based models [17], [18]. However, reconstructing raw pixel values usually fails when normal and anomalous regions share similar values [19]. Another direction is to learn to reconstruct features since they provide more contextual information than raw pixels [5], [19], [20]. With the availability of general-purpose large pretrained networks, there has been a growing interest in learning a reconstruction network to reconstruct features from pretrained networks which have been pretrained on large-scale datasets, *e.g.*, ImageNet, and provide discriminative representations.

Despite the outstanding performance, it has been commonly observed [3], [5], [19] that reconstruction-based methods often encounter the “identity shortcut” issue, a phenomenon of reconstructing anomalies well, due to their uncontrollable generalizability. To alleviate this issue, many strategies [3], [21], [22] have been presented. One simple yet effective strategy is to add perturbations to the input to suppress the reconstruction of anomalies (Fig. 1(a)). For instance, AESc [23] introduces a stain perturbation model to corrupt the image with an ellipse shape of irregular edges. During training, they simply restore the corruption. SCADN [16] generates fixed multi-scale striped masks to erase a part of regions in the input image and learn to reconstruct the missing information. DRAEM [3] obtains promising results by recovering pseudo-anomaly dis-

*Authors contribute equally.

†Corresponding author.

This work is supported by the National Natural Science Foundation of China (No.62302188); Hubei Province Natural Science Foundation (No.2023AFB267); Fundamental Research Funds for the Central Universities (No.2662023XXQD001).

T. Huang, Y. Cheng, J. Xia, X. He and J. Xiang are with the School of Informatics, Huazhong Agricultural University, Wuhan, 430070, China (e-mail: kst0D83@webmail.hzau.edu.cn; hxwxss@webmail.hzau.edu.cn; {xjb, jimmy_xiang, xwhe}@mail.hzau.edu.cn).

R. Yu is with the Computer Science and Engineering Department of J.B. Speed School of Engineering at the University of Louisville, USA (e-mail: rui.yu@louisville.edu).

X. Bai, Y. Cai are with the School of Artificial Intelligence and Automation, Huazhong University of Science and Technology, Wuhan, 430074, China (e-mail: xbai@hust.edu.cn; cyx_hust@hust.edu.cn).

turbed normal images for representation. By perturbing the input, the reconstruction network is forced to learn invariant patterns for reconstruction. Evidently, an effective perturbation scheme is critical. However, prior works simply apply fixed or random masks to perturb input images indiscriminately, regardless of their specific contextual characteristics. In real-world industrial settings with diverse categories and varying shapes and sizes of foreground objects, such strategies easily induce the reconstruction model to overfit the irrelevant background, leading to suboptimal performance.

In this paper, we argue that it is conducive to learning a better reconstruction model by considering sample-specific content and structural priors for perturbation. To this end, we introduce a simple yet effective reconstruction framework named **AGPNet** (see Fig. 2) for unsupervised anomaly detection. The core idea behind our framework is to perturb the normal input according to the importance of each location during training. This approach enables the reconstruction network to pay more attention to those important areas, thereby learning *invariant normal patterns* more compactly and efficiently. To achieve this goal, we carefully design an auxiliary branch that generates attention masks for the noise-adding process (Fig. 1(b)). Specifically, the auxiliary branch combines two important cues to derive the final attention masks. 1) One is the attention maps from the pre-trained feature extraction layers, which provide strong prior on foreground pixels and important localization cues for the reconstruction network. For instance, industrial categories like screws or toothbrushes typically have small foreground areas while textures may have complex structures occupying the whole image. Thus, it would be more efficient and beneficial to pay attention to these important locations. 2) The second cue is the attention maps from the decoder layers of the main branch, which indicates the importance of each location for the reconstruction task. By incorporating this cue, the auxiliary branch dynamically emulates the role of the reconstruction network, thereby preventing training stagnation by perturbing important localizations more aggressively as training progresses. Finally, we perturb the normal input at the main branch with simple Gaussian noise weighted by the final attention masks. This process further helps the framework reason about invariant normal patterns at both low and high levels, ultimately boosting the reconstruction networks to produce discrepancies regarding anomaly samples.

Our framework has several desirable merits. First, it identifies anomalies at high accuracy under both one-class and multi-class settings. By perturbing more aggressively on the important regions, we are in fact attempting to synthesize hard anomalous locations for training, which helps to learn more discriminative and compact boundaries to spot the abnormal patterns. Besides, the attention masks are sample-aware, accommodating images from diverse categories that exhibit different anomaly types. Second, it is more efficient to train. Anomalies in industrial images usually exhibit diverse structures and textures scattered across *any* foreground locations. Some anomalies can be easily identified by reconstructing them based on proximal pixels with similar colors, while anomalies with irregular structures near the contour or local edge pixels pose a challenge for reconstruction. Masking these

critical areas is more conducive and efficient to representation learning for reconstruction. Lastly, it is a concise and effective framework. The whole main branch is just constructed with a pretrained backbone followed by a simple decoder, and the auxiliary branch will be removed after training, incurring no computation cost for inference.

Empirical studies verify that AGPNet greatly improves industrial anomaly detection accuracy. For instance, with only 500 epochs of training, AGPNet achieves P-AUC of 98.0% and I-AUC of 98.7% on MVTec-AD [1] under multi-class setting, outperforming UniAD [5] with 1000 epochs of training by +1.2% and +2.2%, respectively. Our contributions are summarized as follows:

- We present a simple yet effective framework named AGPNet, which integrates a reconstruction network with a novel perturbation scheme leveraging attention mechanisms. It can effectively alleviate “identical shortcut” by applying more targeted perturbations to crucial areas, resulting in superior performance under both multi-class and one-class settings compared with existing state-of-the-art methods.
- We propose to calculate the attention masks based on prior and learnable attention from the reconstruction network. These masks serve to guide the reconstruction network in comprehensively learning normal patterns across diverse industrial images.

II. RELATED WORK

Due to the uncertain and scarce nature of visual anomalies, a dominant direction in this area is to formulate this problem as an unsupervised paradigm, also known as unsupervised anomaly detection. It assumes that all the images in the training set are normal while the test set contains both normal and abnormal images. A great deal of work has been proposed, for more comprehensive surveys, see [24], [25]. Generally, the methods can be broadly divided into three groups: synthesizing-based methods, embedding-based methods, and reconstruction-based methods.

Synthesizing-based methods [3], [10], [26], [27] synthesize anomalies for training. For instance, DRAEM [3] attempts to blend predefined texture images with normal samples. CutPaste [26] simply cuts an image patch and randomly pastes it to another image location. These methods may heavily rely on the quality of the synthesized anomalies. However, due to the uncertainty and unpredictability of anomalies, it is hard and even impossible to synthesize all types of real anomalies with high fidelity.

Embedding-based methods [2], [28]–[30] typically work by first utilizing pretrained models to embed normal images and then employing statistical models to model the normal distributions. During testing, samples are regarded as being abnormal if they are far away from the normal distributions. For instance, PaDiM [2] models the embedded patch features with multivariate Gaussian distribution. PatchCore [28] exploits the memory bank to store nominal features. However, this group of methods generally demands more computational resources to store the normal embeddings for the training set. In addition,

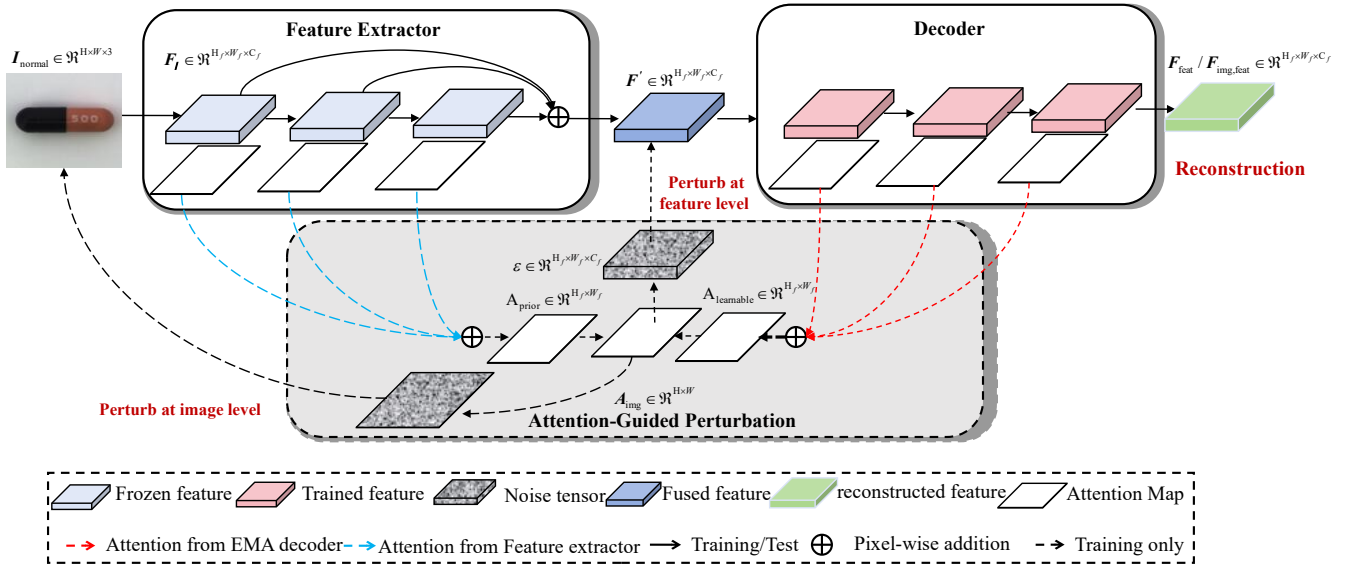


Fig. 2. A framework overview of AGPNet. It consists of two branches, ie, the main reconstruction branch and the attention-guided perturbation branch. During training, given an input normal image I_{normal} , the main reconstruction branch is used for reconstruction, while the perturbation branch aims to generate attention masks based on the main branch for perturbation at both image and feature levels, making the reconstruction network focus on the important local details. During inference, we simply keep the main branch and generate the anomaly map by comparing the input and output of the decoder.

the computing process to identify anomalies during inference is also time-consuming.

Reconstruction-based methods [5], [22], [31], [32] hold the assumption that the model that is trained only on normal data can reconstruct normal samples while finding difficulty in reconstructing anomalous during inference. However, this assumption sometimes is not satisfied because of the strong and uncontrollable generalization of deep neural networks. Therefore, many strategies have been proposed to address this issue. Some methods try to add prior from the images [20], [22], [33] as guidance for reconstructions. For instance, P-Net [22] proposes to feed the structure features into the reconstruction network to guide the reconstruction process. Some methods [23], [34], [35] frame anomaly detection as the image restoration problem by corrupting the selected content in the images and then learning to restore the corruptions. Several methods [36], [37] take the idea of image inpainting by first masking the image randomly and then learning to recover it. Compared with these strategies, our method attempts to add noise at both the feature level and image level according to attention masks. The attention masks, which are computed based on the prior attention from our pretrained model and learnable attention from the decoder, better reflect the local details and their importance. By perturbing these regions more aggressively, our reconstruction network can have a better understanding of the intrinsic and important local normal patterns, which help suppress the anomaly reconstructions effectively.

III. METHOD

Problem Formulation. Following previous works [3], [5], we formulate visual anomaly detection (VAD) as a reconstruction problem. Given a training set $\mathcal{X}_{train} = \{I_{normal}^i\}_{i=1}^N$

comprising *only normal* samples, our main goal is to train a reconstruction model $f(\cdot)$ to accurately identify both pixel and image-level anomalies in a test set $\mathcal{X}_{test} = \{I^j\}_{j=1}^M$ containing both normal and abnormal samples. Note that the problem of VAD can be further divided into two settings: *one-class* and *multi-class*. The one-class setting involves images from the same semantic categories, while the multi-class setting deals with images from diverse semantic categories. The latter is more challenging due to the diverse distributions of different categories, making it difficult to learn compact representations. **Model Overview.** Our framework AGPNet can deal with both one-class and multi-class settings simultaneously. As shown in Fig. 2, it consists of two branches. The main reconstruction branch aims to reconstruct the inputs, while the auxiliary branch aims to generate attention masks to guide the perturbation process for the inputs. With the attention mask as perturbation guidance, the reconstruction network tends to learn invariant normal patterns at those crucial locations. Below we describe each component in detail.

A. Reconstruction Branch

In the main reconstruction branch, we first utilize a frozen backbone to extract image representations and then utilize a lightweight decoder to learn to perform feature reconstructions. The main reconstruction branch is simple and concise, which will be retained for inference.

Feature Extractor. Given an input RGB image $I \in \mathbb{R}^{H \times W \times 3}$, we feed it into a pretrained network $\phi(\cdot)$ and only take a subset of L layer outputs. Any off-the-shelf pre-trained ViT-like model, which relies on attention mechanisms, can readily serve as the feature extractor. In this paper, we follow previous work [38] and adopt DINO [39] as our backbone, which is trained via self-distillation without labels, has demonstrated its

efficacy in generating superior representations for VAD. Note that DINO keeps the resolution fixed along the layer hierarchy, and all the feature maps share the same dimension after packing them into 3D feature maps. We denote $F_l \in \mathbb{R}^{H_f \times W_f \times C_f}$ as the l -th output, and $\sigma(\cdot)$ as the layer normalization function. The representations from specific layers will undergo layer normalization individually, followed by summation:

$$F_{\text{clean}} = \sum_{l=1}^L \sigma(F_l), \quad (1)$$

which will serve as the reconstruction target and be perturbed for further processing by the decoder.

Another important reason to utilize DINO [39] is that it is a vision-transformer-based architecture and its attention weights can be leveraged to generate the attention mask to guide the decoder training with *minimal efforts*. Therefore, in addition to the L outputs, we propose to reuse the associated attention maps, denoted by $A_l \in \mathbb{R}^{H_l \times W_l}$, to provide the important prior cues for the image to guide the training of the decoder. The produced attention weights are taken out and will further be forwarded to the attention-guided perturbation branch for further integration.

Decoder. The decoder aims to decode the pretrained features of *normal* data in the training set. However, without proper design, it easily falls into the “identity shortcut” issue, especially under the multi-class setting. Recently UniAD [5] attempts to alleviate this issue with a learnable-query decoder that incorporates additional learnable queries at each transformer layer. This design incurs additional costs. In our framework, we simply adopt a plain vision-transformer-based decoder thanks to an auxiliary attention-based perturbation branch. During training, the decoder is guided to decode the attention-guided perturbed representations derived from the feature extractor, rather than solely relying on the normal representation. Consequently, the “identity shortcut” issue will be greatly alleviated. Furthermore, our decoder has a more lightweight structure with only four layers, demonstrating strong empirical performance during inference.

B. Attention-Guided Perturbation.

The goal of the auxiliary branch is to perturb normal input for training under the guidance of attention masks. The details are described below.

Attention Mask Generation. To calculate the attention mask, we leverage the attention maps from the feature extractor and the momentum distillation of the decoder, which is formulated as below:

$$\begin{aligned} A_{\text{final}} &= \Phi_{\text{norm}}(A_{\text{prior}}) + \Phi_{\text{norm}}(A_{\text{learn}}) \\ \text{where} \quad &\begin{cases} \Phi_{\text{norm}} := \text{max-min normalization function.} \\ A_{\text{prior}} = \Phi_{\text{aggr}}(\{A_l\}_{l=1}^L) \\ A_{\text{learn}} = \Phi_{\text{aggr}}(\{A_k\}_{k=1}^K) \end{cases} \end{aligned} \quad (2)$$

As discussed earlier, the attention weights from the feature extractor directly reflect the importance of each localization in the feature maps [40]. Therefore, based on the extracted subset of attention weights $\{A_l\}_{l=1}^L$, we compute the prior attention

mask by $A_{\text{prior}} = \Phi_{\text{aggr}}(\{A_l\}_{l=1}^L)$, where Φ_{aggr} denotes the aggregation operation over the attention maps. For simplicity, we only apply element-wise average pooling on the attention maps.

Second, the attention weights within the decoder are learned to aggregate important contextual cues for reconstruction. Hence, we further propose to utilize it for attention mask generation. However, these attention weights fluctuate rapidly with high variance, especially at the beginning of the training. For stabilization, we employ mean-distillation [41], which includes an exponential-moving-average (EMA) version of the decoder as the teacher.

$$\theta_{\text{md}} = \eta \cdot \theta_{\text{md}} + (1 - \eta) \cdot \theta_{\text{dec}} \quad (3)$$

where θ_{md} and θ_{dec} denote the parameters of the teacher and student (*i.e.*, the decoder) models, respectively. η controls the weight assigned to previous teacher parameters. The self-attention weights $\{A_k\}_{k=1}^K$ from the teacher are taken to compute the learnable attention masks by $A_{\text{learn}} = \Phi_{\text{aggr}}(\{A_k\}_{k=1}^K)$. Lastly, we derive the final mask as $A_{\text{final}} = \Phi_{\text{norm}}(A_{\text{prior}}) + \Phi_{\text{norm}}(A_{\text{learn}})$ which will be utilized to guide the following noise-adding process.

Attention-Guided Noise. For unsupervised anomaly detection, synthesized anomalies play a critical role in learning a compact and discriminative boundary to discern normal and abnormal samples. Numerous approaches have been proposed [3], [26] for synthesizing anomalies that closely resemble real ones. Concerning the impracticality of synthesizing all types of real anomalies, we argue that focusing on critical locations and perturbing them at the feature level could be a more efficient strategy. Besides, by perturbing those critical and informative locations, the models are forced to reason the relations across different localizations more comprehensively. To this end, we simply add Gaussian noise weighted by the attention mask in the normal feature space to synthesize the hard abnormal samples. Specifically, a noise tensor $\mathcal{E} \in \mathbb{R}^{H_f \times W_f \times C_f}$ is first generated with each entry simply drawn from an **i.i.d** Gaussian distribution $\mathcal{N}(\mu, \sigma)$. Then we add the noise tensor to the normal features F_{clean} for perturbation based on attention mask A_{final} as follows:

$$F' = F_{\text{clean}} + \mathcal{E} \odot (\alpha(t) \cdot \Phi_{\text{norm}}(A_{\text{final}}) + \beta) \quad (4)$$

where \odot means the elementwise product, $\alpha(t)$ and β control the intensity of adding noise to the features, which linearly increases with the training epochs. β is a hyperparameter. Φ_{norm} denotes the max-min normalization function. The value of $\alpha(t)$ can be calculated by

$$\alpha(t) = \beta \cdot \left(\frac{t}{T} (p - m) + m \right), \quad (5)$$

where p represents the maximum noise intensity, m represents the minimum noise intensity, T represents the maximum training epoch and t represents the current training epoch.

In addition to introducing noise at the feature level, we also incorporate noise at the image level, guided by the attention mask A_{final} , resulting in improved performance. To achieve this, we first upsample A_{final} to match the image dimensions, producing $A_{\text{img}} \in \mathbb{R}^{H \times W}$. Subsequently, we progressively

increase the mask ratio for binarization from 0.6 to 1.0. Gaussian noise is also applied within the masked regions.

C. Loss Function

During training, for each normal image $I_{normal} \in \mathcal{X}_{train}$, we aim to reconstruct its normal features F_{clean} from the perturbed counterparts at both the image and feature levels. Our total loss is derived as

$$L_{total} = \frac{1}{2}(L_{feat} + L_{img,feat}) \quad (6)$$

where L_{feat} indicates reconstruction by perturbing features, and $L_{img,feat}$ represents reconstruction by perturbing image and features at the same time, which are defined below:

$$\begin{cases} L_{feat} = \frac{1}{H_f \times W_f} \text{MSE}(F_{feat}, F_{clean}) \\ L_{img,feat} = \frac{1}{H_f \times W_f} \text{MSE}(F_{img,feat}, F_{clean}) \end{cases} \quad (7)$$

where F_{clean} indicates the features of the pretrained encoder output without noise-added, F_{feat} represents the reconstructed features by perturbing features, and $F_{img,feat}$ means the reconstructed features by perturbing images and features at the same time.

D. Anomaly Map

During inference, we utilize reconstruction errors to calculate the anomaly map. Given an input image $I \in \mathcal{X}_{test}$ from the test set, we first forward it to our framework to calculate pixel-level reconstruction errors in the feature map with L_2 distance. Let $F_q \in \mathbb{R}^{H_f \times W_f \times C_f}$ and $\hat{F}_q \in \mathbb{R}^{H_f \times W_f \times C_f}$ denote the input and output of the reconstruction network, the pixel-level reconstruction error $M \in \mathbb{R}^{H_f \times W_f}$ in the feature space at each pixel location (h, w) is calculated by

$$M_{h,w} = \|F_{h,w} - \hat{F}_{h,w}\|_2 \quad (8)$$

We further upsample M to be the same size as the input image with bilinear interpolation to produce the final anomaly map. For the image level anomaly score, we simply compute the maximum value of the average-pooled M .

IV. EXPERIMENT

A. Experimental Setups

Datasets. *MVTec-AD* [1] is one of the most widely used industrial anomaly detection datasets. It has a training set consisting of 3629 normal images and a test set of 467/1,258 normal/anomaly images. All the images are divided into 15 categories. In this paper, we conduct experiments with two settings. One involves training a single model for all classes (multi-class setting), while the other involves training a separate model for each class (one-class setting). The former is a more efficient yet challenging task.

VisA [42] is another challenging anomaly detection dataset. It has a total of 10,821 images divided into 12 different categories. The training set has 8,659 normal images, and the test set includes 962/1,200 normal/anomaly images.

MVTec-3D [43] is a collection of 4,147 scans obtained through the industrial 3D sensor. It covers 10 different categories, each accompanied by both RGB images and corresponding 3D point cloud data. The training set consists of 2,656 images that include only anomaly-free samples. The test set comprises 1,197 images, which encompass both normal and anomalous samples. In our experiments conducted, only the RGB images were utilized, with the 3D point cloud data not being considered.

Evaluation Metrics. Referring to prior research [2], [3], [5], we report the anomaly detection and localization performance with Image-level and Pixel-level Area Under the Receiver Operating Curve, denoted by I-AUC and P-AUC respectively. We also adopt Per-Region-Overlap [44] to better evaluate model's capability, denoted by PRO.

Implement Details. Each image is resized to 224×224 . The feature extractor is initialized by pre trained DINO(ViT-S-16) [39], which is frozen during training. We employ AdamW [45] optimizer with a weight decay of 1×10^{-4} . We train our framework for 500 epochs on a single GPU (NVIDIA RTX 4090) with a batch size of 32. The learning rate is initially set to 1×10^{-3} and reduced by a factor of 0.1 after 200 epochs. The ratio of added noise at the image level linearly increases from 0.6 to 1.0 from the 100th to 400th epochs. The intensity of added noise α at the feature level linearly increases from 0 to 1.0 from the 1st to 400th epochs. The parameter η in EMA is set to 0.9999, and the mean teacher is updated every 10 steps. In particular, we performed a 32-fold data augmentation (rotate and flip) under a few-shot setting.

B. Anomaly Detection on MVTec-AD

Baseline. We comprehensively evaluated representative methods in both one-class and multi-class settings. In the *multi-class setting*, we first compare our method with two representative one-class approaches: DRAEM [3] and SimpleNet [46], and then compare with methods specifically designed for the multi-class setting, including UniAD [5], RD4AD [8], DiAD [17], ViTAD [47]. Note that all methods are trained under the multi-class scenario. In the *one-class setting*, the compared models includes: RD4AD [8], PatchCore [28], DRAEM [3], DeSTSeg [7], Simplenet [46]. In the *few-shot setting*, We compared our method with some competitive methods and the models designed specifically for few-shot setting, including SPADE [48], PaDiM [2], PatchCore [28], WinCLIP+ [49], RWDA [50], FastRcon [51], PromptAD [52].

Evaluation on MVTec-AD under the multi-class setting.

As shown in Table I, we conducted comprehensive comparative experiments on the MVTec-AD to demonstrate the superiority of our method. It can be observed that applying one-class methods to the multi-class scenario reflects undesirable performance. Furthermore, compared with existing multi-class methods, we outperform all of them, achieving the best 98.7% and 98.0% I-AUC and P-AUC, respectively. ViTAD is a competitive approach, while we outperform it in 12 out of 15 categories in detection capacity, and exceed it in 10 categories for localization performance. In the more challenging PRO metric, our model also achieves the best

TABLE I
ANOMALY DETECTION RESULTS ON MVTEC AD UNDER *multi-class setting*. * DENOTES THE REPRODUCED RESULTS USING THE OFFICIAL CODE. **BOLD** AND UNDERLINE INDICATE THE BEST AND THE SECOND BEST, RESPECTIVELY.

Category	DRÆM* (ICCV 2022)	SimpleNet* (CVPR 2023)	UniAD (NeurIPS 2022)	DiAD (AAAI 2024)	ViTAD (arXiv 2023)	Ours
I-AUC / P-AUC / PRO (%)						
Bottle	97.5 / 87.6 / 80.7	97.7 / 91.2 / 90.6	<u>99.7</u> / 98.1 / 93.2	<u>99.7</u> / 98.4 / -	100.0 / <u>98.8</u> / 94.3	100.0 / 99.1 / 95.0
Cable	57.8 / 71.3 / 40.1	87.6 / 88.1 / 85.4	<u>95.2</u> / <u>97.3</u> / 85.7	94.8 / 96.8 / -	<u>98.5</u> / <u>96.2</u> / <u>90.2</u>	99.7 / 98.0 / 92.9
Capsule	65.3 / 50.5 / 27.3	78.3 / 89.7 / 84.5	86.9 / 98.5 / 89.7	89.0 / 97.1 / -	95.4 / <u>98.3</u> / <u>92.0</u>	<u>93.8</u> / 98.5 / 91.9
Hazelnut	93.7 / 96.9 / 78.7	99.2 / 95.7 / 87.4	<u>99.8</u> / 98.1 / 92.9	99.5 / 98.3 / -	<u>99.8</u> / 99.0 / 95.2	100.0 / <u>98.9</u> / <u>93.6</u>
Metal_nut	72.8 / 62.2 / 66.4	85.1 / 90.9 / 85.2	99.2 / 94.8 / 84.7	99.1 / 97.3 / -	<u>99.7</u> / <u>96.4</u> / <u>92.4</u>	100.0 / <u>95.9</u> / 92.6
Pill	82.2 / 94.4 / 53.9	78.3 / 89.7 / 81.9	93.7 / 95.0 / 94.7	95.7 / 95.7 / -	<u>96.2</u> / 98.7 / <u>95.3</u>	97.6 / <u>98.2</u> / 96.2
Screw	92.0 / 95.5 / 55.2	45.5 / 93.7 / 84.0	87.5 / <u>98.3</u> / <u>94.9</u>	90.7 / 97.9 / -	91.3 / 99.0 / 93.5	91.8 / 99.0 / 95.5
Toothbrush	90.6 / 97.7 / 68.9	94.7 / 97.5 / 87.4	<u>94.2</u> / 98.4 / 88.0	<u>99.7</u> / <u>99.0</u> / -	98.9 / 99.1 / <u>90.9</u>	100.0 / 98.9 / 91.2
Transistor	74.8 / 64.5 / 39.0	82.0 / 86.0 / 83.2	99.8 / 97.9 / 93.3	99.8 / <u>95.1</u> / -	98.8 / 93.9 / 76.8	98.7 / 93.8 / 84.3
Zipper	98.8 / 98.3 / 91.9	99.1 / 97.0 / 90.7	95.8 / 96.8 / <u>91.6</u>	95.1 / 96.2 / -	97.6 / 95.9 / 87.2	99.7 / <u>97.6</u> / 90.5
Carpet	98.0 / 98.6 / 93.1	95.9 / 92.4 / 90.6	<u>99.8</u> / 98.5 / 93.6	99.4 / 98.6 / -	99.5 / <u>99.0</u> / <u>94.7</u>	100.0 / 99.2 / 95.6
Grid	99.3 / 98.7 / 92.1	49.8 / 46.7 / 88.6	98.2 / 96.5 / 91.1	98.5 / 96.6 / -	<u>99.7</u> / 98.6 / <u>95.8</u>	99.9 / 98.9 / 96.3
Leather	98.7 / 97.3 / 88.5	93.9 / 96.9 / 92.7	100.0 / <u>98.8</u> / 96.5	<u>99.8</u> / <u>98.8</u> / -	100.0 / 99.6 / 97.9	100.0 / 97.5 / <u>97.6</u>
Tile	99.8 / 98.0 / 97.0	93.7 / 93.1 / 90.6	99.3 / 91.8 / 78.6	96.8 / 92.4 / -	100.0 / 96.6 / 87.0	100.0 / <u>97.4</u> / <u>90.2</u>
Wood	99.8 / 96.0 / 94.2	95.2 / 84.8 / 76.3	98.6 / 93.2 / 85.0	99.7 / 93.3 / -	98.7 / 96.4 / 88.0	98.9 / 96.6 / 90.2
Mean	88.1 / 87.2 / 71.1	85.1 / 88.9 / 86.5	96.5 / 96.8 / 90.2	97.2 / 96.8 / 90.7	<u>98.3</u> / <u>97.7</u> / <u>91.4</u>	98.7 / 98.0 / 92.9

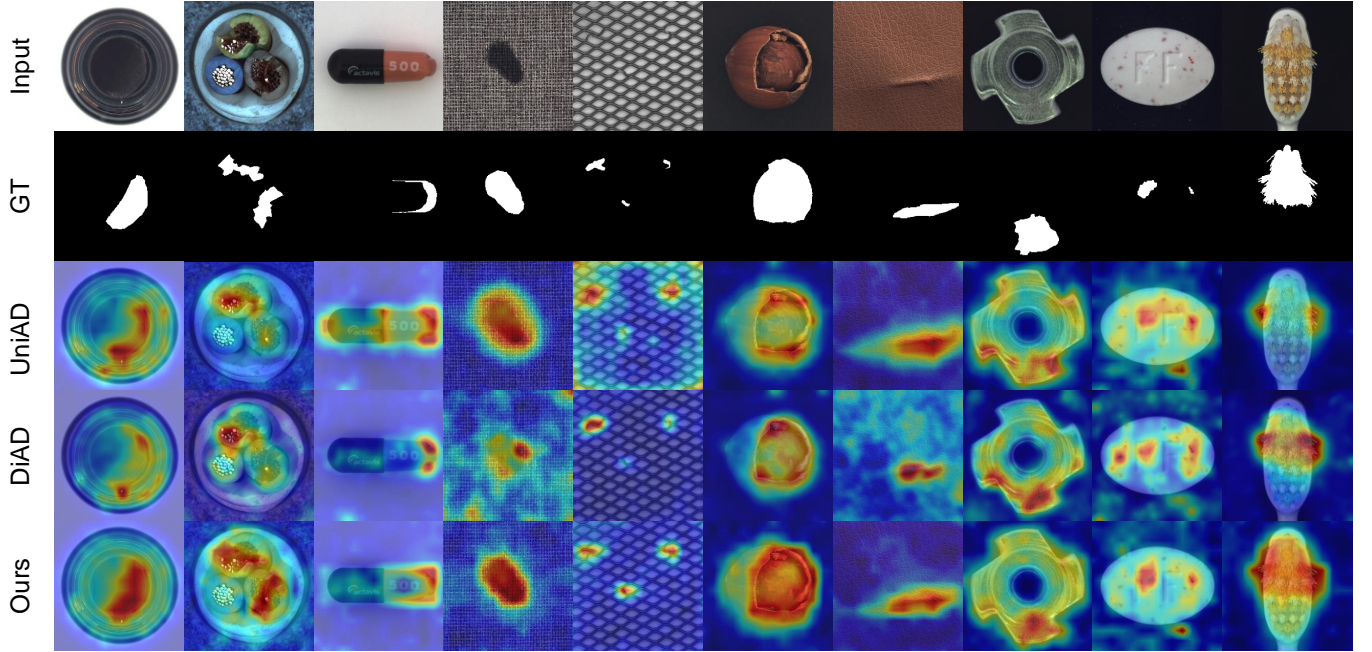


Fig. 3. Qualitative illustration on MVTEC-AD dataset.

performance 92.9%, with a 1.5% improvement over ViTAD. Fig. 3 shows qualitative comparisons between DiAD, UniAD, and our method, indicating that we achieve the most precise anomaly localization results across diverse anomalies.

Evaluation on MVTEC-AD under the one-class setting. As shown in Table II, we can observe that compared with the two synthetic data-based methods, DRAEM [3] and DeSTSeg [28], we outperform them by a large margin. Specifically, compared with DRAEM, we outperform it by 1.2% and 1.0% in I-AUC and P-AUC, respectively. And compared to DeSTSeg, we also bring gains of 0.6% I-AUC and 0.4% P-AUC. Moreover, we achieved the best localization result of 98.3% P-

AUC, while the detection performance is 0.4% lower than SimpleNet, ranking second among previous arts. We argue that although SimpleNet performs well in the one-class setting, its performance significantly drops when adapted to the multi-class scenario (as shown in Table I). Therefore, overall, our model maintains satisfactory performance across both settings.

Evaluation on MVTEC-AD under the few-shot setting. As shown in Table IV, to further demonstrate the generality and potential of our framework, we conduct experiments on MVTEC-AD under the challenging few-shot anomaly detection setups. The experimental results demonstrate the superiority of our method, especially at pixel level. Specifically, our

TABLE II
ANOMALY DETECTION RESULTS ON MVTEC AD UNDER *one-class setting*. * DENOTES THE REPRODUCED RESULTS USING THE OFFICIAL CODE. **BOLD** AND UNDERLINE INDICATE THE BEST AND THE SECOND BEST, RESPECTIVELY.

Category	DRAEM (ICCV 2021)	RD4AD (CVPR 2022)	PatchCore (CVPR 2022)	DeSTSeg (CVPR 2023)	Simplenet (CVPR 2023)	Ours
	I-AUC / P-AUC / PRO (%)					
Bottle	99.2 / 99.1 / -	100.0 / 98.7 / 96.6	100.0 / 98.6 / -	- / 99.2 / -	100.0 / 98.0 / -	100.0 / 99.1 / 94.6
Cable	<u>99.9</u> / 97.6 / -	95.0 / 97.4 / 91.0	99.5 / <u>98.4</u> / -	- / 97.3 / -	94.8 / 96.8 / -	100.0 / 98.7 / 93.9
Capsule	98.5 / 94.3 / -	96.3 / 98.7 / 95.8	<u>98.1</u> / 98.8 / -	- / 99.1 / -	97.7 / <u>98.9</u> / -	97.9 / 98.3 / 90.4
Hazelnut	100.0 / 99.7 / -	99.9 / 98.9 / 95.5	100.0 / 98.7 / -	- / <u>99.6</u> / -	100.0 / 97.9 / -	100.0 / 99.0 / 94.4
Metal_nut	98.7 / 99.5 / -	100.0 / 97.3 / 92.3	100.0 / 98.4 / -	- / 98.6 / -	100.0 / <u>98.8</u> / -	100.0 / 97.0 / 91.5
Pill	<u>98.9</u> / 97.6 / -	96.6 / 98.2 / 96.4	96.6 / 97.4 / -	- / 98.7 / -	99.0 / <u>98.6</u> / -	98.2 / <u>98.6</u> / 96.4
Screw	93.9 / 97.6 / -	97.0 / 99.6 / 98.2	98.1 / <u>99.4</u> / -	- / 98.5 / -	98.2 / 99.3 / -	97.2 / 99.3 / 96.7
Toothbrush	100.0 / 98.1 / -	99.5 / <u>99.1</u> / 94.5	100.0 / 98.7 / -	- / 99.3 / -	99.7 / 98.5	97.2 / 98.9 / 90.3
Transistor	93.1 / 90.9 / -	96.7 / 92.5 / 78.0	100.0 / 96.3 / -	- / 89.1 / -	100.0 / 97.6 / -	99.5 / <u>97.3</u> / 91.3
Zipper	100.0 / 98.8 / -	98.5 / 98.2 / 95.4	99.4 / 98.8 / -	- / 99.1 / -	<u>99.9</u> / <u>98.9</u> / -	99.3 / 97.4 / 93.0
Carpet	97.0 / 95.5 / -	98.9 / 98.9 / 97.0	98.7 / <u>99.0</u> / -	- / 96.1 / -	<u>99.7</u> / 98.2 / -	100.0 / 99.2 / 95.5
Grid	<u>99.9</u> / 99.7 / -	100.0 / <u>99.3</u> / 97.6	98.2 / 98.7 / -	- / 99.1 / -	<u>99.7</u> / 98.8 / -	100.0 / 98.9 / 96.2
Leather	100.0 / 98.6 / -	100.0 / 99.4 / 99.1	100.0 / 99.3 / -	- / 99.7 / -	100.0 / 99.2 / -	100.0 / <u>99.5</u> / 97.7
Tile	99.6 / 99.2 / -	99.3 / 95.6 / 90.6	98.7 / 95.6 / -	- / 98.0 / -	99.8 / 97.0 / -	100.0 / 97.5 / 89.1
Wood	99.1 / 96.4 / -	<u>99.2</u> / 95.3 / 90.9	<u>99.2</u> / 95.0 / -	- / 97.7 / -	100.0 / 94.5 / -	98.8 / <u>96.7</u> / 88.5
Mean	98.0 / 97.3 / -	98.5 / 97.8 / 93.9	99.1 / <u>98.1</u> / <u>93.5</u>	98.6 / 97.9 / -	99.6 / <u>98.1</u> / -	<u>99.2</u> / 98.3 / 93.1

method achieves the best localization performance of 96.2% and 97.3% P-AUC under 2-shot and 4-shot settings. Compared to the competitive method PromptAD, we achieved a 0.8% P-AUC increase under 4-shot settings. Patchcore is a competitive anomaly detection model under the traditional task settings. However, when faced with the more challenging Few-shot setup, our approach outperforms Patchcore with improvements of 6.4%, 7.0%, and 9.0% in I-AUC, and 3.0%, 2.9%, and 3.6% in P-AUC under the 4-shot, 2-shot, and 1-shot setting, respectively. In summary, the results corroborate the method’s generality, particularly its competitive performance demonstrated across various task setups.

C. Anomaly Detection on VisA

Baseline. We further conduct experiments on the challenging VisA dataset and compare with state-of-the-art models including DRAEM [3], UniAD [5], Simplenet [46], DiAD [17], and ViTAD [47].

Evaluation on VisA. As shown in Table III, our method achieves state-of-the-art (SOTA) performance. Compared with UniAD, we outperform it by 6.8% and 3.5% in I-AUC and P-AUC. Specifically, Faced with a competitive model like ViTAD, we outperform it in 10 out of 12 categories for detection and exceed it in 6 categories for localization. Compared with the previous state-of-the-art model (ViTAD), we improve upon it by 1.9%, 0.2% and 0.4% in I-AUC, P-AUC and PRO, respectively. It once again proves the superiority of our method.

D. Anomaly Detection on MVTEC-3D

Baseline. To further verify the superiority of the proposed method, we conduct experiments on the MVTEC-3D dataset and compare it with state-of-the-art models including DRAEM [3], UniAD [5], and DiAD [17].

Evaluation on MVTEC-3D. As illustrated in Table V, our approach outperforms all others across every metric evaluated. Notably, when compared to UniAD, our model demonstrates a considerable advantage, with improvements of 6.0%, 1.5%, and 4.8% in the I-AUC, P-AUC, and PRO, respectively. Compared to the recent diffusion-based method DiAD, our approach has achieved significant improvements in the evaluation metrics, with enhancements of 0.3%, 1.6%, and 5.1% in the I-AUC, P-AUC, and PRO, respectively. These results substantiate the superior performance of our method.

E. Ablation Study

In this subsection, we perform a thorough analysis of our framework on MVTEC-AD under the multi-class setting.

Attention-Guided Noise. Table VI studies the impact of noise addition techniques. We can observe that (1) without perturbing the input, the model achieves 90.5% and 95.5% detection and localization capacities. We believe that the unsatisfactory result is caused by the “identical shortcut” issue, leading the model to fail to reconstruct anomalous patterns to normal. (2) Perturbing the input at the image level in a random manner shows a slight increase in I-AUC. However, adding noise at the feature level results in a significant increase, with gains of +7.5% I-AUC and +2.2% P-AUC, respectively. The phenomenon shows that random noise in the image and feature levels can effectively mitigate the “identical shortcut” issue. (3) When we introduce noise at the image-/feature-level using our Attention-guided method, compared to randomly adding noise at the same levels, we achieve significant benefits. Specifically, in terms of I-AUC, we bring gains of 1.2% (91.9% vs. 90.7%) and 0.3% (98.3% vs. 98.0%), indicating the effectiveness of our strategy. Moreover, applying our strategy to both image and feature levels further enhances model’s ability for anomaly detection and localization, achieving the best 98.7% I-AUC and 98.0% P-AUC. (4) Employing a hybrid noise addition ap-

TABLE III

ANOMALY DETECTION RESULTS ON VISA. * DENOTES THE REPRODUCED RESULTS USING THE OFFICIAL CODE. **BOLD** AND UNDERLINE INDICATE THE BEST AND THE SECOND BEST, RESPECTIVELY.

Category	DRÆM* (ICCV 2021)	UniAD* (NeurIPS 2022)	SimpleNet* (CVPR 2023)	DiAD (AAAI 2024)	ViTAD (arXiv 2023)	Ours
I-AUC / P-AUC / PRO (%)						
PCB1	71.9 / 94.6 / 52.9	92.8 / 93.3 / 64.1	91.6 / 99.2 / 83.6	88.1 / 98.7 / 80.2	<u>95.8</u> / 99.5 / <u>89.6</u>	97.1 / 99.5 / 92.2
PCB2	78.4 / 92.3 / 66.2	87.8 / 93.9 / 66.9	92.4 / 96.6 / 85.7	91.4 / 95.2 / 67.0	<u>90.6</u> / <u>97.9</u> / <u>82.0</u>	94.7 / 98.0 / 82.0
PCB3	76.6 / 90.8 / 43.0	78.6 / 97.3 / 70.6	89.1 / 97.2 / <u>85.1</u>	86.2 / 96.7 / 68.9	<u>90.9</u> / <u>98.2</u> / 88.0	92.1 / 98.3 / 81.4
PCB4	97.3 / 94.4 / 75.7	98.8 / 94.9 / 72.3	97.0 / 93.9 / 61.1	99.6 / 97.0 / 85.0	99.1 / 99.1 / 91.8	<u>99.2</u> / <u>98.7</u> / <u>90.0</u>
Macaroni1	69.8 / 95.0 / 67.0	79.9 / 97.4 / 84.0	<u>85.9</u> / 98.9 / 92.0	85.7 / 94.1 / 68.5	85.8 / <u>98.5</u> / <u>89.2</u>	91.0 / 98.1 / 86.4
Macaroni2	59.4 / 94.6 / 65.3	71.6 / 95.2 / 76.6	68.3 / 93.2 / 77.8	62.5 / 93.6 / 73.1	<u>79.1</u> / 98.1 / 87.2	79.8 / <u>96.9</u> / <u>85.0</u>
Capsules	83.4 / 97.1 / 62.9	55.6 / 88.7 / 43.7	74.1 / 97.1 / 73.7	58.2 / 97.3 / <u>77.9</u>	79.2 / 98.2 / 75.1	78.2 / 98.5 / 78.5
Candles	69.3 / 82.2 / 65.6	94.1 / 98.5 / 91.6	84.1 / 97.6 / 87.6	92.8 / 97.3 / <u>89.4</u>	90.4 / 96.2 / 85.2	<u>93.6</u> / <u>97.7</u> / 88.5
Cashew	81.7 / 80.7 / 38.5	92.8 / 98.6 / 87.9	88.0 / 98.9 / 84.1	91.5 / 90.9 / 61.8	87.8 / 98.5 / 78.8	94.1 / 99.2 / 87.7
Chewing gum	93.7 / 91.0 / 41.0	<u>96.3</u> / <u>98.8</u> / 81.3	<u>96.4</u> / 97.9 / <u>78.3</u>	99.1 / 94.7 / 59.5	94.9 / 97.8 / 71.5	96.1 / 98.9 / 73.5
Fryum	89.1 / 92.4 / 69.5	83.0 / 95.9 / 76.2	88.4 / 93.0 / 85.1	89.8 / 97.6 / 81.3	94.3 / <u>97.5</u> / 87.8	<u>93.7</u> / <u>97.5</u> / <u>86.8</u>
Pipe fryum	82.8 / 91.1 / 61.9	94.7 / 98.9 / 91.5	90.8 / 98.5 / 83.0	96.2 / 99.4 / 89.9	97.8 / 99.5 / 94.7	98.4 / 99.4 / 94.4
Mean	79.1 / 91.3 / 59.1	85.5 / 95.9 / 75.6	87.2 / 96.8 / 81.4	86.8 / 96.0 / 75.2	<u>90.5</u> / <u>98.2</u> / <u>85.1</u>	92.3 / 98.4 / 85.5

TABLE IV

ANOMALY DETECTION RESULTS ON MVTEC UNDER *few shot setting*. **BOLD** AND UNDERLINE INDICATE THE BEST AND THE SECOND BEST, RESPECTIVELY.

Method	1-shot	2-shot	4-shot
I-AUC / P-AUC (%)			
SPADE (arXiv 2020)	81.0 / 91.2	82.9 / 92.0	84.8 / 92.7
PaDiM (ICPR 2020)	76.6 / 89.3	78.9 / 91.3	80.4 / 92.6
PatchCore (CVPR 2022)	83.4 / 92.0	86.3 / 93.3	88.8 / 94.3
WinCLIP+ (CVPR 2023)	93.1 / 95.2	94.4 / 96.0	<u>95.2</u> / 96.2
RWDA (BMVC 2023)	<u>93.3</u> / -	94.0 / -	94.5 / -
FastRcon (ICCV 2023)	- / -	91.0 / 95.9	94.2 / <u>97.0</u>
PromptAD (CVPR 2024)	94.6 / 95.9	95.7 / 96.2	96.6 / 96.5
Ours	<u>92.4</u> / <u>95.6</u>	93.3 / 96.2	<u>95.2</u> / 97.3

TABLE V

ANOMALY DETECTION RESULTS ON MVTEC-3D. * DENOTES THE REPRODUCED RESULTS USING THE OFFICIAL CODE. **BOLD** AND UNDERLINE INDICATE THE BEST AND THE SECOND BEST, RESPECTIVELY.

Method	DRÆM* (ICCV 2021)	UniAD* (NeurIPS 2022)	DiAD (AAAI 2024)	Ours
I-AUC	65.2	78.9	84.6	84.9
P-AUC	93.2	<u>96.5</u>	96.4	98.0
PRO	55.0	<u>88.1</u>	87.8	92.9

proach only achieves suboptimal performance, further proving the superiority of our attention-guided strategy.

Backbone. To prove the generality of our method, we conduct comprehensive experiments using various backbones. As shown in Table VII, We employed two mainstream CNN-based backbones (Wide-Resnet-50 [53] and EfficientNet-b4 [54]) and two mainstream ViT-based backbones (CLIP [55] and DINO [39]) for our experiments. Compared to other mainstream anomaly detection frameworks, our method maintains competitive performance while using the same pre-trained backbones. Specifically, comparing to the ViTAD-CLIP, our method achieves a 23.4% improvement in I-AUC and a 14.2% improvement in P-AUC. When facing SimpleNet with WideResNet50, our method outperform with a 2.3% increase

in I-AUC and a 4.5% increase in P-AUC. The results fully demonstrate the generality of the proposed attention-guided perturbation method.

Multi-Layer Features. Table VIII studies the impact of using multi-layer features. It can be observed that when utilizing deep features, the model demonstrates robust detection capacities, achieving 97.8% I-AUC. In contrast, employing shallow features exhibits desirable localization abilities. Overall, integrating both shallow and deep features yields optimal performance.

Mean Teacher Decoder. Table VIII validates the effectiveness of the Mean Teacher decoder. Using the decoder of the reconstructed model to generate attention maps serves as the baseline. Introducing the Mean Teacher decoder results in an improvement of 0.3% for detection and 0.1% for localization, respectively. The experiments prove that the introduction of the Mean Teacher decoder can effectively overcome the high variance of learnable attention weights at the beginning of training.

Easy-to-Hard Noise Addition. Recall that in Sec. 3.3, we use a hyperparameter α to control the noise intensity at the feature level. Table IX explores the impact of noise intensity. The experiments indicate that Easy-to-hard noise with suitable intensity helps the model to model the target distribution and achieve the best performance. Compared with fixed noise of different intensities, the I-AUC and P-AUC are slightly improved(0.1%-0.4%).

Attention Map. Table IX ablates two components for the final attention mask. We can observe that 1) using A_{prior} alone to guide the noise tensor already gives us satisfactory performance, and 2) only A_{learn} guiding the noise tensor can achieve results close to the optimal. 3) Finally, combining both obtains the highest performance. It demonstrates the effectiveness of combining learnable and prior attention for the final attention mask.

F. Efficiency Comparison with SoTAs on MVtec-AD

In addition to model performance, the efficiency of the model is a critical concern for practical applications. We eval-

TABLE VI

ABLATION STUDIES ON ATTENTION-GUIDED NOISE. ‘-’ MEANS NO NOISE IS ADDED. ‘R’ INDICATES ADDING RANDOM NOISE. ‘A’ DENOTES ADDING ATTENTION-GUIDED NOISE.

Noise Type Image/Feature-level	No Noise -/-	Only Random			Only Attention			Hybrid	
		R/-	-/R	R/R	A/-	-/A	A/A	A/R	R/A
I-AUC (%)	90.5	90.7	98.0	97.7	91.9	98.3	98.7	98.3	98.6
P-AUC (%)	95.5	95.5	97.7	97.8	96.0	97.7	98.0	97.8	97.8

TABLE VII

ABLATION STUDIES ON BACKBONES AND COMPARE WITH THE PREVIOUS METHODS IN MULTI-CLASS SETTING.

Backbone	Method	I-AUC/P-AUC(%)
WideResNet-50	SimpleNet	85.1 / 88.9
	Ours	87.4 / 93.4
EfficientNet-b4	UniAD	96.5 / 96.8
	Ours	97.0 / 96.7
CLIP(ViT-B)	ViTAD-CLIP	71.2 / 81.6
	Ours	94.6 / 95.8
DINO(ViT-S)	ViTAD	98.3 / 97.7
	Ours	98.7 / 98.0

TABLE VIII

ABLATION STUDIES ON MULTI-LEVEL FEATURES AND MEAN DISTILLATION. “M.T.D” INDICATES GENERATING ATTENTION MAPS WITH MEAN DISTILLATION, WHILE “W.O.” MEANS WITHOUT USING MEAN DISTILLATION.

Components Options	Multi-layer					Mean Teacher	
	f_{11}	f_2, f_5	f_8, f_{11}	f_2, f_5, f_8, f_{11}		w.o.	M.T.D
I-AUC (%)	97.7	98.1	98.1	98.7		98.4	98.7
P-AUC (%)	97.8	97.0	97.8	98.0		97.9	98.0

uate the efficiency of various methods on a single RTX4090 GPU with a batch size of 32 using Learnable Parameters (M), Floating Point Operations (FLOPs), and Frames Per Second (FPS). As demonstrated in Table X, our method ranks second in terms of both Learnable Parameters and FPS, while achieving the highest FLOPs. These results indicate that our proposed method effectively balances efficiency and performance, exhibiting strong potential for deployment on end-user devices.

V. LIMITATION

Similar to other unsupervised anomaly methods, the proposed method may be sensitive to noisy samples. In future investigations, it is worthy of focusing on framework robustness especially when abnormal samples corrupt the training set. Furthermore, our framework mainly demonstrates the superior performance in industrial anomaly detection, while its generality in other areas such as medical anomaly detection and video anomaly analysis deserves more extensive investigation.

VI. CONCLUSION

In this paper, we have proposed a simple yet effective reconstruction-based framework AGPNet to alleviate the issue of ‘identical shortcut’ for visual anomaly detection. It consists of a reconstruction branch for reconstruction and an auxiliary branch that aims to generate an attention mask for perturbations. To accommodate various samples across diverse

TABLE IX

ABLATION STUDIES ON NOISE INTENSITY α AT FEATURE-LEVEL AND ATTENTION MAP. ‘D’ INDICATES JUST USING THE A_{LEARN} TO GUIDE THE NOISE TENSOR, ‘L’ DENOTES JUST USING THE A_{PRIOR} TO GUIDE THE NOISE TENSOR, AND ‘B’ MEANS COMBINING A_{PRIOR} AND A_{LEARN} TO GUIDE THE NOISE TENSOR.

Components Options	Noise Intensity α at Feature-level				Attention map		
	0.5	1.0	1.5	0-1.0	L	D	B
I-AUC (%)	98.5	98.6	98.3	98.7	98.4	98.6	98.7
P-AUC (%)	97.9	97.9	97.9	98.0	97.9	97.9	98.0

TABLE X

EFFICIENCY COMPARISON OF DIFFERENT METHODS

Method	Learnable Parameters(M)	FLOPs(G)	FPS
DRÆM (ICCV 2021)	97.42	198.15	95.17
UniAD (NeurIPS 2022)	7.48	6.46	286.92
DeSTSeg (CVPR 2023)	32.37	30.67	386.76
SimpleNet (CVPR 2023)	3.94	18.34	63.66
Ours	4.42	5.63	326.65

categories, the attention mask is based on prior attention weights from the frozen feature extractor and mean-distillation of the decoder. Extensive experiments have been done to prove that our framework obtains superior performance under both one and multi-class settings. In the future, we plan to experiment with foundation models to provide attention masks as a prior for perturbations, as well as explore robust models under noisy data settings.

REFERENCES

- [1] P. Bergmann, M. Fauser, D. Sattlegger, and C. Steger, “Mvtec ad—a comprehensive real-world dataset for unsupervised anomaly detection,” in *CVPR*, 2019, pp. 9592–9600.
- [2] T. Defard, A. Setkov, A. Loesch, and R. Audigier, “Padim: a patch distribution modeling framework for anomaly detection and localization,” in *ICPR*, 2021, pp. 475–489.
- [3] V. Zavrtanik, M. Kristan, and D. Skočaj, “Draem-a discriminatively trained reconstruction embedding for surface anomaly detection,” in *ICCV*, 2021, pp. 8330–8339.
- [4] P. Bergmann, S. Löwe, M. Fauser, D. Sattlegger, and C. Steger, “Improving unsupervised defect segmentation by applying structural similarity to autoencoders,” in *Proceedings of the 14th International Joint Conference on Computer Vision, Imaging and Computer Graphics Theory and Applications*, 2019.
- [5] Z. You, L. Cui, Y. Shen, K. Yang, X. Lu, Y. Zheng, and X. Le, “A unified model for multi-class anomaly detection,” *NeurIPS*, vol. 35, pp. 4571–4584, 2022.
- [6] P. Bergmann, M. Fauser, D. Sattlegger, and C. Steger, “Uninformed students: Student-teacher anomaly detection with discriminative latent embeddings,” in *CVPR*, 2020, pp. 4183–4192.
- [7] X. Zhang, S. Li, X. Li, P. Huang, J. Shan, and T. Chen, “Destseg: Segmentation guided denoising student-teacher for anomaly detection,” in *CVPR*, 2023, pp. 3914–3923.
- [8] H. Deng and X. Li, “Anomaly detection via reverse distillation from one-class embedding,” in *CVPR*, 2022, pp. 9737–9746.

- [9] H. M. Schlüter, J. Tan, B. Hou, and B. Kainz, “Natural synthetic anomalies for self-supervised anomaly detection and localization,” in *ECCV*, 2022, pp. 474–489.
- [10] V. Zavrtanik, M. Kristan, and D. Skočaj, “Dsr – a dual subspace re-projection network for surface anomaly detection,” 2022.
- [11] Y. Liang, J. Zhang, S. Zhao, R. Wu, Y. Liu, and S. Pan, “Omni-frequency channel-selection representations for unsupervised anomaly detection,” *IEEE TIP*, 2023.
- [12] D. Gong, L. Liu, V. Le, B. Saha, M. R. Mansour, S. Venkatesh, and A. v. d. Hengel, “Memorizing normality to detect anomaly: Memory-augmented deep autoencoder for unsupervised anomaly detection,” in *ICCV*, 2019, pp. 1705–1714.
- [13] D. T. Nguyen, Z. Lou, M. Klar, and T. Brox, “Anomaly detection with multiple-hypotheses predictions,” in *ICML*, 2019, pp. 4800–4809.
- [14] M. Sabokrou, M. Khalooei, M. Fathy, and E. Adeli, “Adversarially learned one-class classifier for novelty detection,” in *CVPR*, 2018, pp. 3379–3388.
- [15] J. Kim, K. Jeong, H. Choi, and K. Seo, “Gan-based anomaly detection in imbalance problems,” in *Computer Vision–ECCV 2020 Workshops: Glasgow, UK, August 23–28, 2020, Proceedings, Part VI 16*, 2020, pp. 128–145.
- [16] X. Yan, H. Zhang, X. Xu, X. Hu, and P.-A. Heng, “Learning semantic context from normal samples for unsupervised anomaly detection,” in *AAAI*, vol. 35, 2021, pp. 3110–3118.
- [17] H. He, J. Zhang, H. Chen, X. Chen, Z. Li, X. Chen, Y. Wang, C. Wang, and L. Xie, “Diad: A diffusion-based framework for multi-class anomaly detection,” *arXiv preprint arXiv:2312.06607*, 2023.
- [18] X. Zhang, N. Li, J. Li, T. Dai, Y. Jiang, and S.-T. Xia, “Unsupervised surface anomaly detection with diffusion probabilistic model,” in *ICCV*, 2023, pp. 6782–6791.
- [19] Z. You, K. Yang, W. Luo, L. Cui, Y. Zheng, and X. Le, “Adtr: Anomaly detection transformer with feature reconstruction,” in *International Conference on Neural Information Processing*, 2022, pp. 298–310.
- [20] Y. Shi, J. Yang, and Z. Qi, “Unsupervised anomaly segmentation via deep feature reconstruction,” *Neurocomputing*, vol. 424, pp. 9–22, 2021.
- [21] M. Haselmann, D. P. Gruber, and P. Tabatabai, “Anomaly detection using deep learning based image completion,” in *2018 17th IEEE international conference on machine learning and applications (ICMLA)*, 2018, pp. 1237–1242.
- [22] K. Zhou, Y. Xiao, J. Yang, J. Cheng, W. Liu, W. Luo, Z. Gu, J. Liu, and S. Gao, “Encoding structure-texture relation with p-net for anomaly detection in retinal images,” in *ECCV*, 2020, pp. 360–377.
- [23] A.-S. Collin and C. De Vleeschouwer, “Improved anomaly detection by training an autoencoder with skip connections on images corrupted with stain-shaped noise,” in *ICPR*, 2021, pp. 7915–7922.
- [24] J. Liu, G. Xie, J. Wang, S. Li, C. Wang, F. Zheng, and Y. Jin, “Deep industrial image anomaly detection: A survey,” *Machine Intelligence Research*, vol. 21, no. 1, pp. 104–135, 2024.
- [25] J. Zipfel, F. Verworn, M. Fischer, U. Wieland, M. Kraus, and P. Zschech, “Anomaly detection for industrial quality assurance: A comparative evaluation of unsupervised deep learning models,” *Computers & Industrial Engineering*, vol. 177, p. 109045, 2023.
- [26] C.-L. Li, K. Sohn, J. Yoon, and T. Pfister, “Cutpaste: Self-supervised learning for anomaly detection and localization,” in *CVPR*, 2021, pp. 9664–9674.
- [27] H. M. Schlüter, J. Tan, B. Hou, and B. Kainz, “Natural synthetic anomalies for self-supervised anomaly detection and localization,” in *ECCV*, 2022, pp. 474–489.
- [28] K. Roth, L. Pemula, J. Zepeda, B. Schölkopf, T. Brox, and P. Gehler, “Towards total recall in industrial anomaly detection,” in *CVPR*, June 2022, pp. 14 318–14 328.
- [29] W. Liu, H. Chang, B. Ma, S. Shan, and X. Chen, “Diversity-measurable anomaly detection,” in *CVPR*, 2023, pp. 12 147–12 156.
- [30] J. Bae, J.-H. Lee, and S. Kim, “Pni: industrial anomaly detection using position and neighborhood information,” in *ICCV*, 2023, pp. 6373–6383.
- [31] V. Zavrtanik, M. Kristan, and D. Skočaj, “Reconstruction by inpainting for visual anomaly detection,” *PR*, vol. 112, p. 107706, 2021.
- [32] H. M. Schlüter, J. Tan, B. Hou, and B. Kainz, “Natural synthetic anomalies for self-supervised anomaly detection and localization,” in *European Conference on Computer Vision*, 2022, pp. 474–489.
- [33] Y. Xia, Y. Zhang, F. Liu, W. Shen, and A. L. Yuille, “Synthesize then compare: Detecting failures and anomalies for semantic segmentation,” in *Computer Vision–ECCV 2020: 16th European Conference, Glasgow, UK, August 23–28, 2020, Proceedings, Part I 16*, 2020, pp. 145–161.
- [34] F. Ye, C. Huang, J. Cao, M. Li, Y. Zhang, and C. Lu, “Attribute restoration framework for anomaly detection,” *IEEE TMM*, vol. 24, pp. 116–127, 2020.
- [35] T. Liu, B. Li, X. Du, B. Jiang, L. Geng, F. Wang, and Z. Zhao, “Fair: Frequency-aware image restoration for industrial visual anomaly detection,” *arXiv preprint arXiv:2309.07068*, 2023.
- [36] Z. Li, N. Li, K. Jiang, Z. Ma, X. Wei, X. Hong, and Y. Gong, “Super-pixel masking and inpainting for self-supervised anomaly detection,” in *BMVC*, 2020.
- [37] V. Zavrtanik, M. Kristan, and D. Skočaj, “Reconstruction by inpainting for visual anomaly detection,” *PR*, vol. 112, p. 107706, 2021.
- [38] T. Reiss, N. Cohen, E. Horwitz, R. Abutbul, and Y. Hoshen, “Anomaly detection requires better representations,” 2022.
- [39] M. Caron, H. Touvron, I. Misra, H. Jégou, J. Mairal, P. Bojanowski, and A. Joulin, “Emerging properties in self-supervised vision transformers,” in *ICCV*, 2021, pp. 9650–9660.
- [40] M. D. Zeiler and R. Fergus, “Visualizing and understanding convolutional networks,” in *Computer Vision–ECCV 2014: 13th European Conference, Zurich, Switzerland, September 6–12, 2014, Proceedings, Part I 13*, 2014, pp. 818–833.
- [41] A. Tarvainen and H. Valpola, “Mean teachers are better role models: Weight-averaged consistency targets improve semi-supervised deep learning results,” 2018.
- [42] Y. Zou, J. Jeong, L. Pemula, D. Zhang, and O. Dabeer, “Spot-the-difference self-supervised pre-training for anomaly detection and segmentation,” in *ECCV*, 2022, pp. 392–408.
- [43] P. Bergmann, X. Jin, D. Sattlegger, and C. Steger, “The mvtec 3d-ad dataset for unsupervised 3d anomaly detection and localization,” *arXiv preprint arXiv:2112.09045*, 2021.
- [44] P. Bergmann, M. Fauser, D. Sattlegger, and C. Steger, “Uninformed students: Student-teacher anomaly detection with discriminative latent embeddings,” in *2020 IEEE/CVF Conference on Computer Vision and Pattern Recognition (CVPR)*. IEEE, Jun. 2020. [Online]. Available: <http://dx.doi.org/10.1109/CVPR42600.2020.00424>
- [45] I. Loshchilov and F. Hutter, “Decoupled weight decay regularization,” 2019. [Online]. Available: <https://arxiv.org/abs/1711.05101>
- [46] Z. Liu, Y. Zhou, Y. Xu, and Z. Wang, “SimpleNet: A simple network for image anomaly detection and localization,” in *CVPR*, 2023, pp. 20 402–20 411.
- [47] J. Zhang, X. Chen, Y. Wang, C. Wang, Y. Liu, X. Li, M.-H. Yang, and D. Tao, “Exploring plain vit reconstruction for multi-class unsupervised anomaly detection,” *arXiv preprint arXiv:2312.07495*, 2023.
- [48] N. Cohen and Y. Hoshen, “Sub-image anomaly detection with deep pyramid correspondences,” *arXiv preprint arXiv:2005.02357*, 2020.
- [49] J. Jeong, Y. Zou, T. Kim, D. Zhang, A. Ravichandran, and O. Dabeer, “Winclip: Zero-/few-shot anomaly classification and segmentation,” in *Proceedings of the IEEE/CVF Conference on Computer Vision and Pattern Recognition*, 2023, pp. 19 606–19 616.
- [50] M. Tamura, “Random word data augmentation with clip for zero-shot anomaly detection,” *arXiv preprint arXiv:2308.11119*, 2023.
- [51] Z. Fang, X. Wang, H. Li, J. Liu, Q. Hu, and J. Xiao, “Fastrecon: Few-shot industrial anomaly detection via fast feature reconstruction,” in *Proceedings of the IEEE/CVF International Conference on Computer Vision*, 2023, pp. 17 481–17 490.
- [52] X. Li, Z. Zhang, X. Tan, C. Chen, Y. Qu, Y. Xie, and L. Ma, “Promptad: Learning prompts with only normal samples for few-shot anomaly detection,” in *Proceedings of the IEEE/CVF Conference on Computer Vision and Pattern Recognition*, 2024, pp. 16 838–16 848.
- [53] K. He, X. Zhang, S. Ren, and J. Sun, “Deep residual learning for image recognition,” 2015. [Online]. Available: <https://arxiv.org/abs/1512.03385>
- [54] M. Tan and Q. V. Le, “Efficientnet: Rethinking model scaling for convolutional neural networks,” 2020. [Online]. Available: <https://arxiv.org/abs/1905.11946>
- [55] A. Radford, J. W. Kim, C. Hallacy, A. Ramesh, G. Goh, S. Agarwal, G. Sastry, A. Askell, P. Mishkin, J. Clark *et al.*, “Learning transferable visual models from natural language supervision,” in *ICML*, 2021, pp. 8748–8763.